Kinetics and interaction studies of anti-tetraspanin antibodies and ICAM-1 with extracellular vesicle subpopulations using continuous flow quartz crystal microbalance biosensor

Liangsupree, Thanaporn

2022-06-15

http://hdl.handle.net/10138/344190
https://doi.org/10.1016/j.bios.2022.114151

Kinetics and interaction studies of anti-tetraspanin antibodies and ICAM-1 with extracellular vesicle subpopulations using continuous flow quartz crystal microbalance biosensor

Thanaporn Liangsupree [a], Evgen Multia [a], Patrik Forssén [b], Torgny Fornstedt [b], Marja-Liisa Riekkola [a,*]

[a] Department of Chemistry, P.O. Box 55, FI-00014, University of Helsinki, Finland
[b] Department of Engineering and Chemical Sciences, Karlstad University, SE-651 88, Karlstad, Sweden

ARTICLE INFO

ABSTRACT

Continuous flow quartz crystal microbalance (QCM) was utilized to study binding kinetics between EV subpopulations (exomere- and exosome-sized EVs) and four affinity ligands: monoclonal antibodies against tetraspanins (anti-CD9, anti-CD63, and anti-CD81) and recombinant intercellular adhesion molecule-1 (ICAM-1) or CD54 protein. High purity $CD9^+$, $CD63^+$, and $CD81^+$ EV subpopulations of <50 nm exomeres and 50–80 nm exosomes were isolated and fractionated using our recently developed on-line coupled immunoaffinity chromatography – asymmetric flow field-flow fractionation system. Adaptive Interaction Distribution Algorithm (AIDA), specifically designed for the analysis of complex biological interactions, was used with a four-step procedure for reliable estimation of the degree of heterogeneity in rate constant distributions. Interactions between exomere-sized EVs and anti-tetraspanin antibodies demonstrated two interaction sites with comparable binding kinetics and estimated dissociation constants K_d ranging from nM to fM. Exomeres exhibited slightly higher affinity compared to exosomes. The highest affinity with anti-tetraspanin antibodies was achieved with $CD63^+$ EVs. The interaction of EV subpopulations with ICAM-1 involved in cell internalization of EVs was also investigated. EV – ICAM-1 interaction was also of high affinity (nM to pM range) with overall lower affinity compared to the interactions of anti-tetraspanin antibodies and EVs. Our findings proved that QCM is a valuable label-free tool for kinetic studies with limited sample concentration, and that advanced algorithms, such as AIDA, are crucial for proper determination of kinetic heterogeneity. To the best of our knowledge, this is the first kinetic study on the interaction between plasma-derived EV subpopulations and anti-tetraspanin antibodies and ICAM-1.

1. Introduction

Extracellular vesicles (EVs) are heterogeneous nanosized lipid particles (50–3000 nm) released from cells that can be found in various biological fluids. EVs are involved in intercellular signaling and regulating pathological and physiological processes (Gonda et al., 2019). Among other EV subpopulations, exosomes (50–150 nm) having endosomal origins have gathered increasing attention in recent years, not only due to their potential roles in communication in the cellular microenvironment but also due to their associations with pathological processes and various diseases (Kalluri and LeBleu, 2020). In addition to exosomes, a smaller EV subpopulation called exomere (under 50 nm) has only recently been identified by asymmetric flow-field flow

fractionation (AF4 or AsFlFFF) (Multia et al., 2020; Zhang et al., 2018) and thus requires further and more extensive studies to shed light on its properties, interactions, and functions.

Several studies have shown that proteins expressed on EV surfaces, such as tetraspanins (e.g., CD9, CD63, and CD81) and adhesion molecules, facilitate cell-to-cell communication (Gonda et al., 2019; Meldolesi, 2018; Termini and Gillette, 2017). Tetraspanins, a family of membrane proteins, participate in various important cellular processes, including cell adhesion, membrane fusion, and signaling events (Andreu and Yáñez-Mó, 2014; Hemler, 2005). Moreover, multiple EV isolation and characterization techniques, including immunoaffinity purification, flow cytometry, enzyme-linked immunosorbent assay, and Western blot, utilize antibodies targeting the tetraspanin proteins on EV surfaces

---

(Liangsupree et al., 2021a; Willms et al., 2018). In addition to tetraspanins, the intercellular adhesion molecules 1 (ICAM-1) or CD54 protein, a class of transmembrane glycoproteins, plays an essential role in immune response and EV uptake by cells, including anchoring and internalization (Gonda et al., 2019; Müller, 2019). ICAM-1 also takes part in the cellular uptake of drug-loaded exosomes, highlighting its importance in drug delivery applications (Yong et al., 2019). Further studies for such interactions can also be beneficial for further development of EV isolation and characterization techniques. More importantly, studies of interactions between EVs and ICAM-1 could provide better understanding of cellular uptake, especially for EV subpopulations having different sizes and origins.

Quartz crystal microbalance (QCM) is a mass-sensitive biosensor which has been proven an excellent tool for simple and label-free characterization and kinetic studies of nanosized bioparticles (Liangsupree et al., 2019; Multia et al., 2017; Suthar et al., 2020). Among other techniques used to study interaction kinetics, QCM was reported to offer very high target selectivity in affinity-based biosensing applications (Lim et al., 2020). Moreover, even the femtomolar (fM) detection limit could be achieved with QCM (Premaratne et al., 2017). These advantages make QCM an excellent technique to study interactions of EV subpopulations that are often isolated in relatively small quantities.

In this study, the continuous flow QCM was successfully used to elucidate binding kinetics between affinity ligands (monoclonal anti-tetraspanin antibodies (anti-CD9, CD63, and CD81) and recombinant ICAM-1) and $CD9^+$, $CD63^+$, and $CD81^+$ EV subpopulations of <50 nm exomeres and 50–80 nm exosomes, isolated from human blood plasma using our previously developed on-line coupled immunoaffinity chromatography – asymmetric flow field-flow fractionation system (Multia et al., 2020). Their interaction kinetics were analyzed using Adaptive Interaction Distribution Algorithm (AIDA) (Forssén et al., 2018). To the extent of our knowledge, this is the first study on interactions between plasma-derived EV subpopulations of different sizes and affinity ligands, particularly ICAM-1 which has been known to be involved in EV internalization.

2. Material and methods

2.1. Chemicals and materials

Chemicals and materials used in this study are listed in Supplementary material.

2.2. Instrumentation

Instrumentation used in this study is listed in Supplementary material.

2.3. Isolation and characterization of EV subpopulations

Isolation and fractionation of EV subpopulations were performed using our developed on-line and automated IAC – AsFlFFF system (Multia et al., 2020) (Fig. 1). The isolated and fractionated EV subpopulations were characterized with several techniques as reported in our previous studies (Liangsupree et al., 2021b; Multia et al., 2019, 2020). More information on EV isolation, fractionation, and characterization is included in Supplementary material.

2.4. Preparation of affinity ligands and extracellular vesicle subpopulations

Preparation of affinity ligand solutions and EVs can be found in Supplementary material.

2.5. Continuous flow quartz crystal microbalance kinetics and interaction studies of EV subpopulations

2.5.1. Immobilization of affinity ligands on the LNB-carboxyl sensor chip

Anti-CD9, anti-CD63, and anti-CD81 antibodies and ICAM-1 were separately immobilized onto the LNB-carboxyl sensor chips via amine coupling according to our previous studies (Liangsupree et al., 2019; Multia et al., 2017) with slight modifications. The LNB-carboxyl sensor
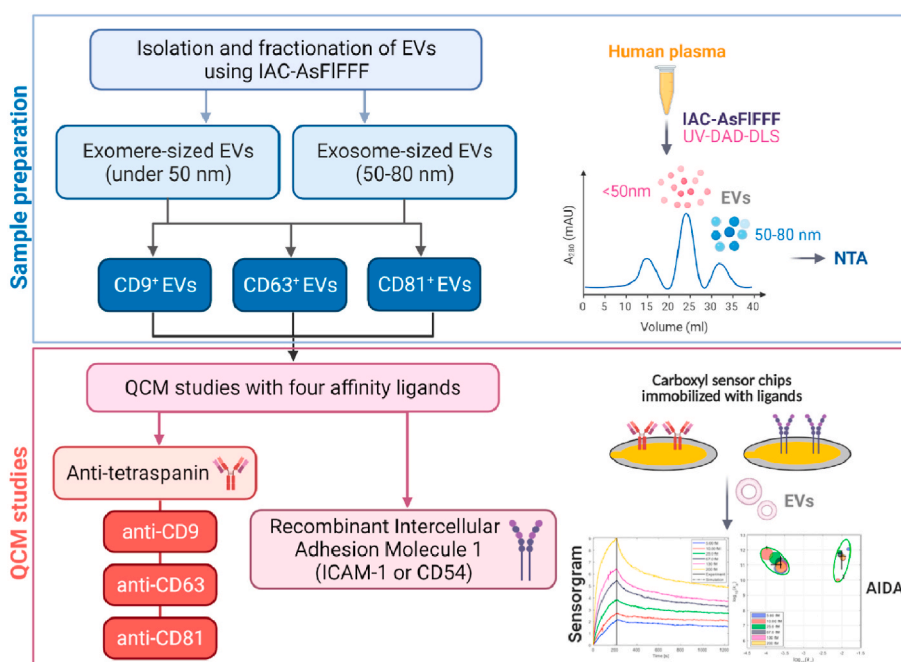

Fig. 1. Simplified experimental workflow for QCM studies of interactions between EV subpopulations and affinity ligands including monoclonal anti-tetraspanin antibodies and ICAM-1. The study started with isolation, fractionation, and characterization of plasma-derived $CD9^+$, $CD63^+$, and $CD81^+$ (exomere- and exosome-sized) EV subpopulations using IAC-AsFlFFF followed by QCM interaction studies and calculation of dissociation constants using AIDA.

chips utilize AT-cut quartz crystal (the cut is performed at an angle of 35° 15′ from the Z-axis) with the fundamental frequency of approximately 10 MHz (D'Ulivo et al., 2010; Vrhovac et al., 2021). Briefly, the LNB-carboxyl sensor chip was pre-wetted *ex situ* with MilliQ water (20 μL) and left to stand for an hour at room temperature. Thereafter, the sensor chip was inserted into the instrument and left to stabilize. The entire immobilization process was performed in 4-(2-hydroxyethyl)-1-piperazineethanesulfonic acid (HEPES) running buffer ($I = 10$ mM, 150 mM NaCl, 0.005% TWEEN 20, pH 7.4) at 25°C with a flow rate of 10 μL/min using automated C-Fast software. Surface activation was performed with two consecutive injections of a freshly mixed 1-ethyl-3-(3-dimethylaminopropyl) carbodiimide hydrochloride (EDC-HCl) (0.2 M) and sulfo-N-hydroxy-succinimide (S-NHS) (0.05 M) solutions (1:1, v/v) (100 μL and 300 s each). The ligand solution (80 μg/mL) was injected twice (100 μL and 300 s each). Lastly, the remaining carboxyl groups on the chip surface were deactivated with two injections of 1 M ethanolamine solution (pH 9.0) (100 μL and 300 s each). Attana Evaluation Software was used to visualize the recorded sensorgrams.

2.5.2. QCM interaction studies of EV subpopulations

The interactions between EV subpopulations: CD9^{+}, CD63^{+}, CD81^{+} of exomere-sized (under 50 nm) and exosome-sized (50–80 nm) and affinity ligands (anti-tetraspanin antibodies: anti-CD9, anti-CD63, and anti-CD81, and ICAM-1) were studied using QCM at a flow rate of 25 μL/min at 37.0°C. The binding buffer was phosphate buffered saline (PBS) (pH 7.4, $I = 10$ mM, 137 mM NaCl, and 2.7 mM KCl). Prior to the sample injection, the binding buffer (90 μL) was injected using the automated C-Fast software to equilibrate the sensor chip surface with a dissociation time of 10 s. The diluted EV samples (90 μL) were consequently injected and allowed to dissociate for 1000 s. The sensor chip was regenerated using NH_4OH (0.15 M, 90 μL) and sodium dodecyl sulfate (SDS) (1%, 90 μL), whenever necessary, and re-equilibrated with the binding buffer (90 μL). Note that the penetration depth of a quartz crystal with 10 MHz fundamental frequency under water loading at 37°C reported in the literature is approximately 180 nm (Galli Marxer et al., 2003), making this QCM setting applicable for interaction studies between EVs of under 50 nm and 50–80 nm with anti-tetraspanins and ICAM-1.

2.5.3. Reliable estimation of rate constants

By using a common framework that can represent several different adsorption processes, one can analyze and compare systems. For steady state adsorption, one can represent the process using a so-called Adsorption Energy Distribution (Fornstedt, 2010) and for non-steady-state kinetic data (as here), one can represent the process using a so called Rate Constant Distribution (RCD) (Forssén et al., 2018; Gutgsell et al., 2022). An RCD consists of bivariate distributions of association rates and dissociation rate constants and was here calculated using a recently developed numerical algorithm, Adaptive Interaction Distribution Algorithm (AIDA) (Forssén et al., 2018; Zhang et al., 2017). AIDA is used for QCM data here, but it should be noted that it can also handle data from other types of biosensor systems such as surface plasmon resonance (Gutgsell et al., 2022).

The reliable estimation of rate constants by AIDA was made in a four-step evaluation process. Firstly, dissociation curves were plotting by $\ln(R/R_0)$ versus time. The characteristics of these plots determine the system heterogeneity, i.e., a linear dissociation curve indicates a single interaction, while a concave dissociation curve implies that there is more than one interaction in the system. In the case of heterogeneous binding, the RCD is calculated separately for each obtained sensorgram to estimate the number of interactions in the system (step 2). RCD can simply be regarded as a decomposition of a kinetic process parallel reactions, regardless of the true mechanism, like an arbitrary signal that can be decomposed into harmonic base functions by using a Fourier transform regardless of how the signal was generated. An RCD representation of the system requires the association curve that is an increasing concave function and the dissociation curve that is a decreasing convex function. It should be noted that the RCD calculation uses an ill-posed inverse problem, and the solution is greatly dependent on the type and amount of regularization applied. The third step of AIDA was to perform fitting to the sensorgrams one by one using the number of interactions calculated in the earlier step. The fourth and final step of AIDA is to cluster the rate constants estimated in the previous steps to allow visualization of overall kinetic characteristics of the system. It is worth mentioning that one of the advantages of this approach is that it is applicable for deteriorating systems, e.g., loss of affinity ligands on sensor chip overtime. Deterioration will result in outlier rate constants, and by using this approach they can be removed from consideration a posteriori. Sensorgrams were corrected with blank injections of PBS prior to the estimation of kinetic rate constants whenever necessary.

3. Results and discussion

This section describes and discusses results obtained for the interactions between exomere- and exosome-sized EV subpopulations and four different affinity ligands, including monoclonal anti-tetraspanin antibodies and ICAM-1 using continuous flow QCM. The EV subpopulations were isolated and fractionated from human plasma with the IAC-AsFlFFF system, including monolithic columns separately immobilized with anti-CD9, anti-CD63, and anti-CD81 antibodies which aimed to bind CD9, CD63, and CD81 tetraspanins enriched on EVs of endosomal origins (Caby et al., 2005; Witwer and Théry, 2019). The acquired EV subpopulations were named according to the target tetraspanin surface proteins, i.e., exomere- and exosome-sized CD9^{+} (isolated from the anti-CD9 monolithic disk), CD63^{+} (from the anti-CD63 monolithic disk), and lastly CD81^{+} EVs (from the anti-CD81 monolithic disk), following terms used in our previous study (Liangsupree et al., 2021b). It is important to note that these EV terms do not indicate that each specific EV subpopulation only contains a single type of tetraspanin. For instance, in the case of CD9^{+} EVs, other tetraspanins in addition to CD9 may also be expressed on the CD9^{+} EV surfaces. The overlapping presence of tetraspanins on plasma-derived EVs has also been widely reported in literature (Karimi et al., 2018; Tutanov et al., 2020). Finally, the obtained interaction results were analyzed by our previously developed numerical algorithm AIDA.

3.1. Interactions between EV subpopulations and monoclonal anti-tetraspanin antibodies

The first section of this present study explored interactions between monoclonal anti-tetraspanin antibodies, namely anti-CD9, anti-CD63, and anti-CD81 antibodies with EV subpopulations isolated and fractionated using IAC-AsFlFFF. The exomere- and exosome-sized EV fractions were characterized during the on-line isolation and fractionation processes with a UV-VIS spectrophotometer, dynamic light scattering, and diode array detectors as reported in our previous studies (Liangsupree et al., 2021b; Multia et al., 2020), and their particle concentrations were measured by nanoparticle tracking analysis (NTA) (Table S1). More detailed characterization of EV subpopulations with Raman spectroscopy and scanning electron microscopy is found in (Liangsupree et al., 2021b). The interactions between EV subpopulations were studied using sensor chips separately immobilized with monoclonal anti-CD9, anti-CD63, or anti-CD81, representing antibodies commonly used for isolation and characterization of EVs in the size range of exosomes, on LNB-carboxyl sensor chips at the physiological temperature of 37.0°C. The acquired sensorgrams (Figs. S1–S5) were processed and analyzed using AIDA which allows clear visualization of binding kinetics information, including number of interaction sites and clustered association k_a and dissociation k_d rate constants as shown in Figs. 2–5. Dissociation constants K_d were calculated and plotted in Fig. 6. More detailed information on rate constants together with the dissociation constants is available in Table S2.
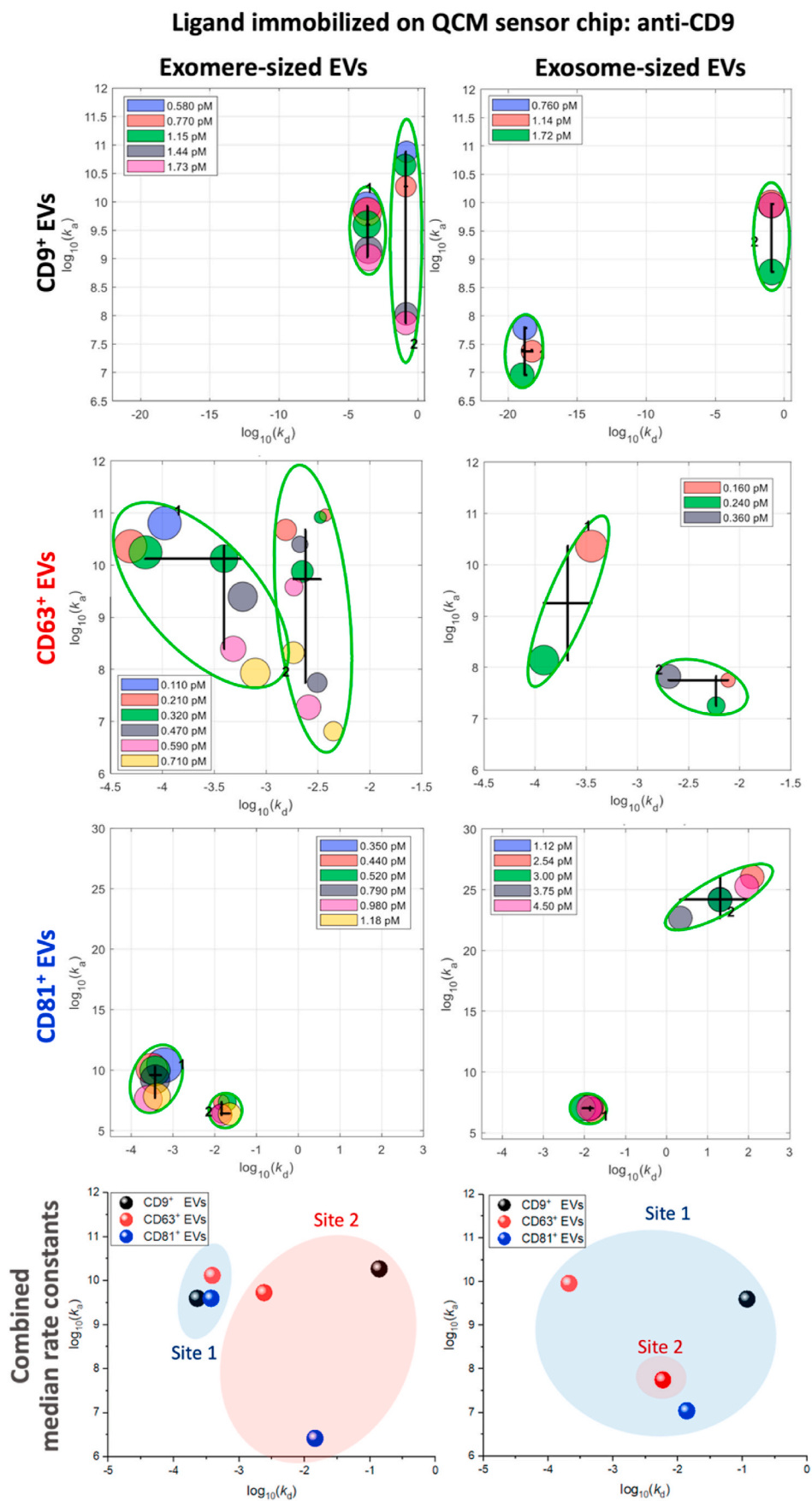
Fig. 2. Clustered rate constants for the interactions between anti-CD9 and CD9$^+$, CD63$^+$, and CD81$^+$ EVs of exomere- (left panel) and exosome-sized (right panel). The combined average rate constants were plotted in the lowest panel. For more information on rate constants, see Table S2.

Fig. 3. Clustered rate constants for the interactions between anti-CD63 and CD9^{+}, CD63^{+}, and CD81^{+} EVs of exomere- (left panel) and exosome-sized (right panel). The combined average rate constants were plotted in the lowest panel. For more information on rate constants, see Table S2.
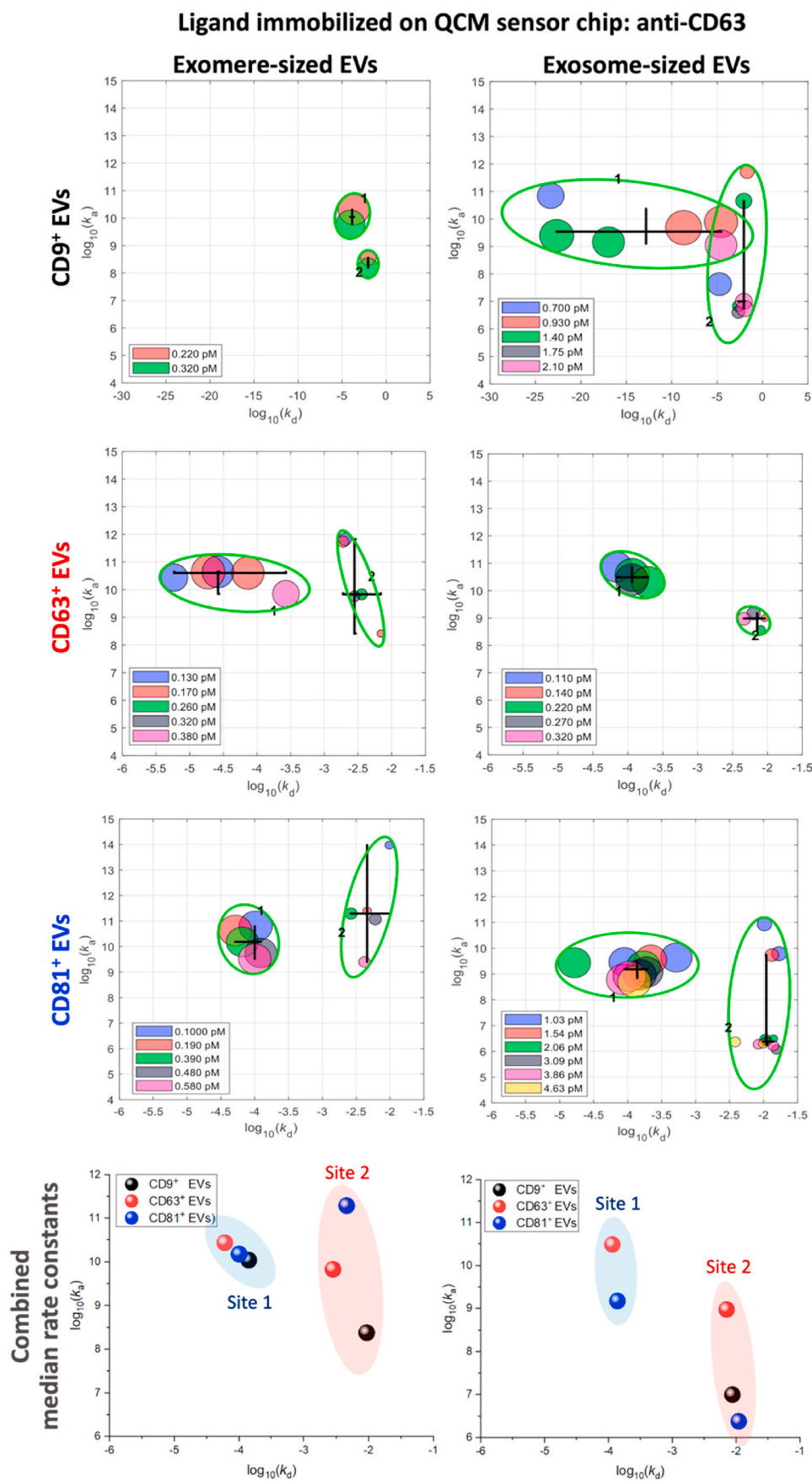
Fig. 4. Clustered rate constants for the interactions between anti-CD81 and CD9$^+$, CD63$^+$, and CD81$^+$ EVs of exomere- (left panel) and exosome-sized (right panel). The combined average rate constants were plotted in the lowest panel. For more information on rate constants, see Table S2.
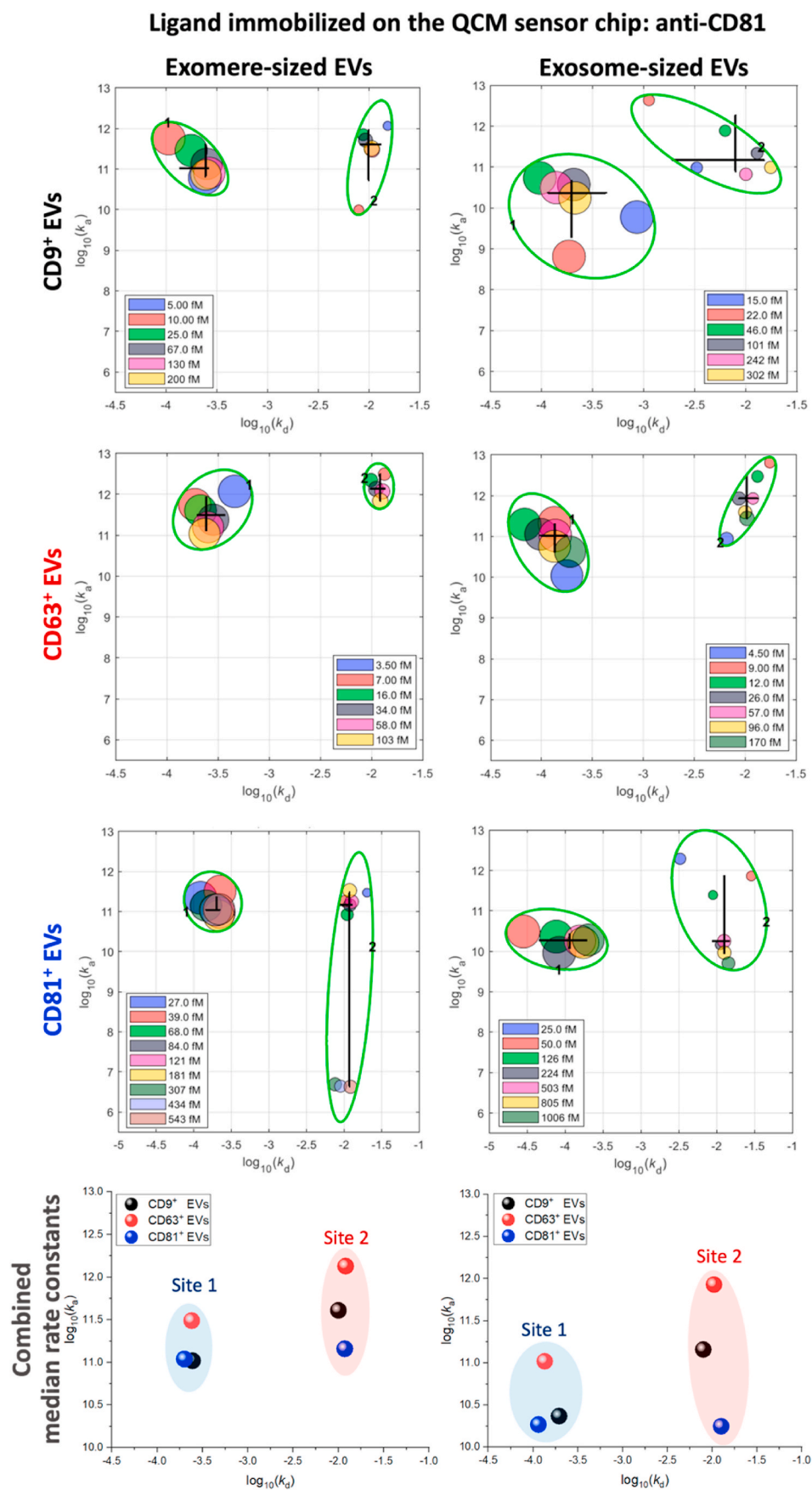
Fig. 5. Clustered rate constants for the interactions between ICAM-1 and CD9^{+}, CD63^{+}, and CD81^{+} EVs of exomere- (left panel) and exosome-sized (right panel). The combined average rate constants were plotted in the lowest panel. For more information on rate constants, see Table S2.
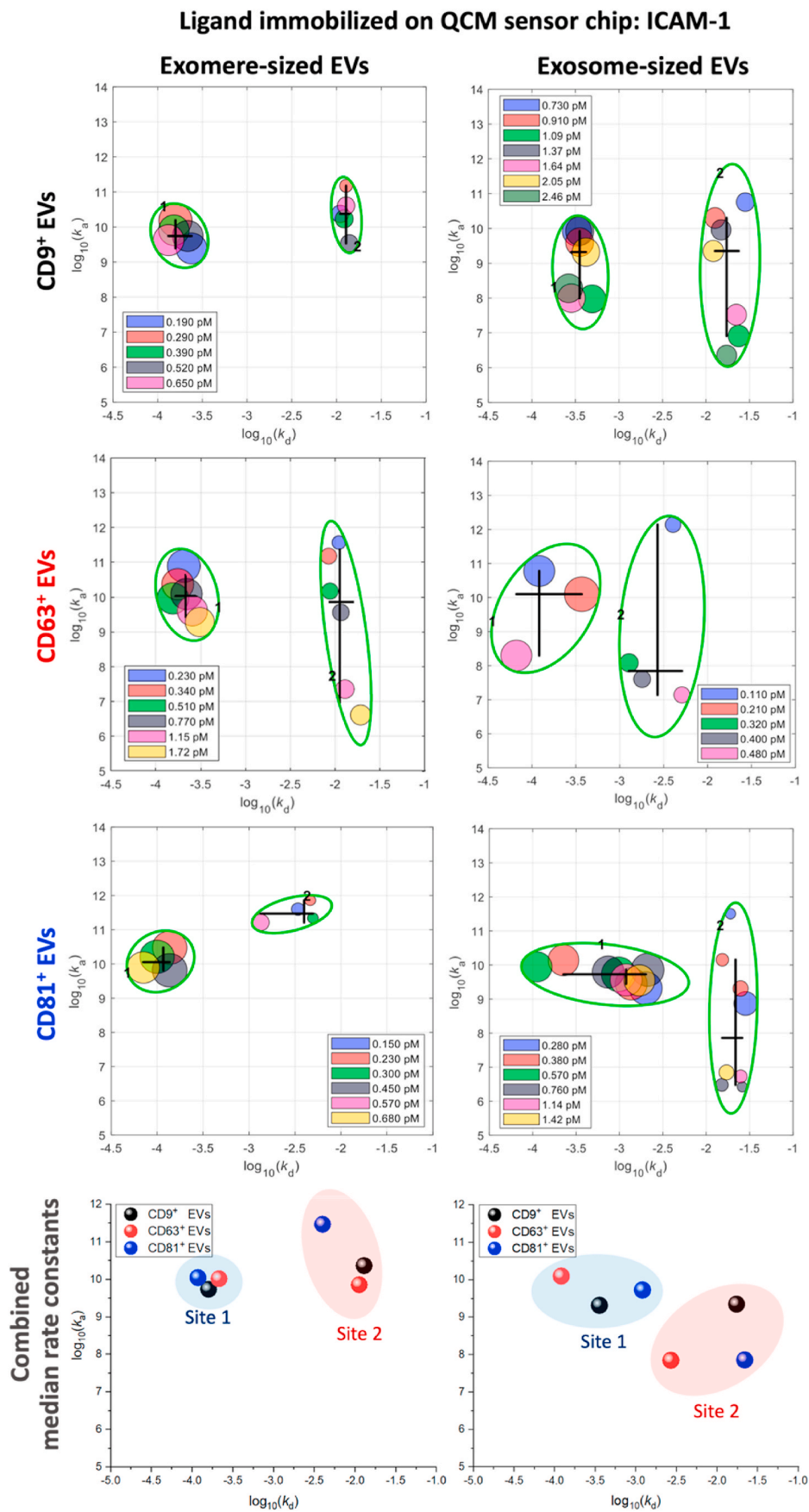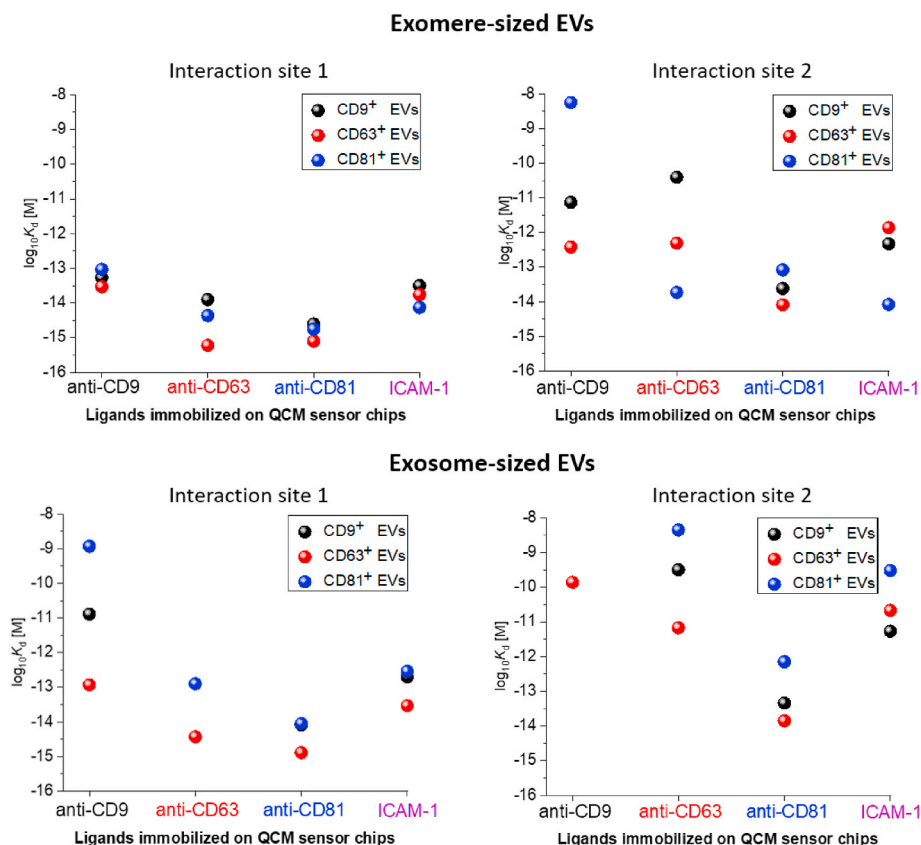
Fig. 6. Dissociation constants (logarithmic scale) calculated by AIDA for interaction sites 1 and 2 for exomere-sized EVs (top panel) and exosome-sized EVs (bottom panel). For more information on rate constants, see Table S2.

The first part of the study was done to elucidate the interactions between anti-CD9 and EV subpopulations. A suitable interaction model was selected based on the dissociation graph (Fig. S1) which deviated from the reference diagonal, indicating heterogeneous binding. Further analysis by AIDA resulted in rate constant distribution with two interaction sites (Fig. S1). As a result, the two-site interaction model was chosen as the most suitable model for data analysis. Interaction site 1 was identified as the major interaction with over 60% contribution to the whole system for all EVs as shown in Fig. 2. The calculated $\log K_d$ values for site 1 for exomere-sized CD9$^+$, CD63$^+$, and CD81$^+$ EVs were comparable ($\log K_d$ = approximately -13 M) (Fig. 6). Interaction site 2 represented weaker interaction affinities compared to site 1, with the estimated $\log K_d$ of -11.13, -12.42, and -8.25 M for exomere-sized CD9$^+$, CD63$^+$, and CD81$^+$ EVs, respectively. For exosome-sized EVs, their overall affinity was lower than those determined for exomere-sized EVs as also shown in Figs. 2 and 6. The interaction site 1 of exosome-sized CD9$^+$, CD63$^+$ and CD81$^+$ EVs resulted in $\log K_d$ of -10.89, -12.93 and -8.93 M, respectively. Lower affinity was achieved for interaction site 2 with an estimated $\log K_d$ of -9.86 M for exosome-sized CD63$^+$ EVs, while the K_d of exosome-sized CD9$^+$ and CD81$^+$ EVs were outliers and excluded from the combined plots in Figs. 2 and 6. As opposed to the exomere-sized EVs which resulted in similar affinity toward anti-CD9, noticeable differences in affinity were found among the exosome-sized EVs, with CD63$^+$ demonstrating highest affinity ($\log K_d$ = -13.53 M, site 1), followed by CD9$^+$ ($\log K_d$ = -13.27 M, site 1) and CD81$^+$ EVs ($\log K_d$ = -13.03 M, site 1) (Fig. 6).

Secondly, the interactions between anti-CD63 and EV subpopulations were studied, and their clustered rate constant distributions are displayed in Fig. 3. Similar to the interactions between anti-CD9 and EVs, the two-site interaction model was used. Interaction site 1 was accounted for over 75% of the total interactions for all EVs studied. The $\log K_d$ for site 1 for exomere-sized CD9$^+$, CD63$^+$, and CD81$^+$ EVs were

-13.90, -15.22, and -14.36 M, respectively (Fig. 6). Interaction site 2 showed slightly lower affinity ($\log K_d$ = -10.41, -12.31, and -13.73 M for CD9$^+$, CD63$^+$, and CD81$^+$ EVs, respectively) as also seen in the clustered plots (Fig. 3). Exosome-sized EVs resulted in higher dissociation constants for both interaction sites (Fig. 6), thus lower affinity, compared to the exomere-sized EVs. This finding was similar to the interaction between EVs and anti-CD9. The highest affinity for the anti-CD63 and EV subpopulations was achieved from CD63$^+$ exomere-sized EVs ($\log K_d$ = -15.22 M, site 1). This could be because the same anti-CD63 antibody was used as an immunoaffinity ligand for separation in IAC.

We further investigated the interactions between EVs and anti-CD81. As seen in Fig. 4, all exomere-sized EVs resulted in similar rate constants toward anti-CD81. The overall k_a values for interaction site 1 of exomere-sized EVs were slightly higher compared to those of the exosome-sized EVs (Table S2). This was also the case for interaction site 2 and other interactions between EVs and anti-tetraspanin antibodies. The observation could be caused by a slightly larger size of exosome-sized EVs (50–80 nm) compared to the exomere-sized EVs (under 50 nm). A similar finding related to size and interaction speed was previously noticed for the interaction between anti-apolipoprotein B-100 and lipoproteins in which larger lipoproteins (a mixture of very-low-density and intermediate-density lipoproteins) showed slightly lower k_a than smaller low-density lipoprotein (Multia et al., 2017).

The highest affinity for anti-CD81 — EV interactions was again achieved with the exomere-sized CD63$^+$ EVs ($\log K_d$ = -15.10 M). However, the calculated $\log K_d$ for other EV subpopulations were similar in the range of approximately -14 to -15 M for site 1 and -12 to -14 M for site 2 (Fig. 6). Comparable to the interaction with anti-CD63, exosome-sized EVs gave overall slightly lower affinity toward anti-CD81 than exomere-sized EVs except for CD63$^+$ EVs which showed very similar affinity regardless of the sizes. It was found that lyophilization of EV subpopulations used for anti-CD81 was not necessary for pre-

concentration, as lower concentration ranges of the fractionated samples were already sufficient to obtain satisfactory sensorgram response. To our surprise, the $\log K_d$ values were comparable to those of the lyophilized samples, suggesting that the lyophilization did not significantly affect binding characteristics of anti-tetraspanin antibodies toward EV subpopulations.

Overall interactions of EVs with anti-tetraspanin antibodies resulted in very high affinity with the majority of K_d being over 10^{-9} M (Table S2). Among EV subpopulations, CD63$^+$ exomere-sized EVs interacted most strongly with all anti-tetraspanin antibodies, implying that the CD63$^+$ EVs most likely contained CD9 and CD81 on their surfaces along with CD63. The highest affinity system was the interaction between CD63$^+$ exomere-sized EVs and anti-CD63. Both exomere- and exosome-sized EV subpopulations gave overall very similar affinity (average $K_d = 10^{-14}$ M, site 1, and 10^{-10} M, site 2) (Table S2). The high affinity of the interactions was already observed during the experiments, as in most experiments, the desorption of EVs from the antibodies on the sensor chip surface could not be achieved only with alkaline pH (NH$_4$OH, pH 11.5), but SDS (1%, w/v) was also required to get complete baseline regeneration. Such high affinity (10^{-11} to 10^{-12} M or pM range) has been reported in other studies involving interactions between monoclonal antibodies against different receptors, including cell receptors (Xie et al., 2005) and immunoglobulins (Stubenrauch et al., 2013). Moreover, compared to kinetic studies of other nanosized particles, such as the interactions between lipoproteins and anti-apolipoprotein B-100 with similar experimental settings and conditions (Liangsupree et al., 2019; Multia et al., 2017), in this study the affinity of anti-tetraspanin antibodies and EV subpopulations was higher (nM range for lipoproteins and pM range for EV subpopulations). An even higher affinity range (fM) was experimentally observed for most of the interactions labeled as site 1 in this study. Although generally the experimentally reported K_d values for monoclonal antibody – antigen interactions are mostly in a nM or pM range, a fM range has also been observed before (Liu et al., 2015). The binding kinetics in the fM range might be due to multivalent ligand binding. However, more studies are needed to confirm this assumption. Above all, each monoclonal anti-tetraspanin antibody used in this study exhibited very strong binding, being suitable for applications involving the use of these antibodies, such as immunoaffinity isolation and immunosensors.

3.2. Interactions between EV subpopulations and ICAM-1

ICAM-1 or CD54 are expressed on cell membranes and EV surfaces and take part in anchoring and internalization of exosomes (Gonda et al., 2019; Morelli et al., 2004). It has been reported that ICAM-1 interacts with lymphocyte function-associated antigen 1 (LFA-1) (Eniola-Adefeso et al., 2009) also during exosome uptake by dendritic cells (Hao et al., 2007). In addition, exosomes utilize CD9 and CD81 tetraspanins to aid the internalization processes (Gonda et al., 2019; Zech et al., 2012). This study aimed to further understand the interaction between ICAM-1 and exomere- and exosome-sized CD9$^+$, CD63$^+$, and CD81$^+$ EV subpopulations.

Similar to the interactions with anti-tetraspanin antibodies, a two-site interaction model was used for the analysis of kinetic data from the interaction between EV subpopulations and ICAM-1 (Fig. 5). The interactions were found to have relatively high affinity with the estimated $\log K_d$ of approximately -11 to -13 M for CD9$^+$ and CD63$^+$ EVs and -10 to -14 M for CD81$^+$ EVs (Fig. 6). Among EV subpopulations, the highest affinity with ICAM-1 was found with exomere-sized CD81$^+$ EVs ($\log K_d = -14.13$ M, site 1). Overall, exomere-sized EVs demonstrated a higher affinity toward ICAM-1 compared to the exosome-sized EVs. The same trend was also observed in the case of anti-tetraspanin antibody – EV interactions. However, ICAM-1 exhibited slightly lower affinity compared to anti-tetraspanin antibodies, possibly due to the strong and specific binding of monoclonal antibodies. Moreover, since LFA-1 is an integrin normally present on EV surface (Reina and Espel, 2017), one of

the receptors for ICAM-1 – EV interaction could be LFA-1. The estimated K_d reported in the literature for the interactions between ICAM-1 and LFA-1 was in a nM range (Vitte et al., 2004). A higher affinity measured in this study could also be due to other receptors present on the EV surface.

4. Conclusions

Continuous flow quartz crystal microbalance combined with Adaptive Interaction Distribution Algorithm (AIDA) was utilized to study binding kinetics between EV subpopulations (CD9$^+$, CD63$^+$, and CD81$^+$) of exomeres under 50 nm and exosomes between 50 and 80 nm and four affinity ligands, including monoclonal anti-tetraspanin antibodies (anti-CD9, anti-CD63, and anti-CD81) and recombinant ICAM-1 or CD54. The interactions between anti-tetraspanin antibodies and EV subpopulations resulted in two interaction sites of very high affinity ranging from nM to fM range. Exomere-sized EVs demonstrated higher affinity compared to exosome-sized EVs. Based on the estimated dissociation constants, the strongest affinity was achieved with the interaction between exomere-sized CD63$^+$ EVs and their corresponding anti-CD63 ligand (fM range). Similar findings were obtained for ICAM-1 in which very high affinity in the range of nM to fM was achieved with exomere-sized EVs where exomere-sized CD81$^+$ EVs interacted the strongest with ICAM-1. However, overall ICAM-1 – EV subpopulation interactions were weaker compared to anti-tetraspanin antibody interactions with EV subpopulations.

Interaction studies between EV subpopulations and affinity ligands as well as the estimation of dissociation constant is a challenging task due to multiple factors, including the estimation of available binding sites on the EV subpopulations at low EV subpopulation concentrations. QCM combined with powerful algorithm (AIDA) proved to be a valuable tool for comparative estimation of biomacromolecular binding characteristics even at fM concentrations of analytes. The rate constant distribution plots allowed descriptive and visual illustration of affinity in the biological system. Moreover, QCM sensor chip surfaces could be regenerated multiple times, and experiments were done in an automated manner. The system allowed cost-effective kinetic studies and minimal operator involvement, making this setup a more suitable approach for kinetic and interaction studies compared to, for instance, enzyme-linked immunosorbent assays and potentiometric titration.

Credit authorship contribution statement

This manuscript was written throughout the contributions of all authors.

Declaration of competing interest

The authors declare the following financial interests/personal relationships which may be considered as potential competing interests: Patent application (no. 20192643.3-1020).

Appendix A. Supplementary data

Supplementary data to this article can be found online at https://doi.org/10.1016/j.bios.2022.114151.

References

Andreu, Z., Yáñez-Mó, M., 2014. Front. Immunol. 5, 442.

Caby, M.-P., Lankar, D., Vincendeau-Scherrer, C., Raposo, G., Bonnerot, C., 2005. Int. Immunol. 17, 879–887.

D'Ulivo, L., Saint-Guirons, J., Ingemarsson, B., Riekkola, M.-L., 2010. Anal. Bioanal. Chem. 396, 1373–1380.

Eniola-Adefeso, O., Huang, R.B., Smith, C.W., 2009. Ann. Biomed. Eng. 37, 737–748.

Fornstedt, T., 2010. J. Chromatogr. A 1217, 792–812.

Forssén, P., Multia, E., Samuelsson, J., Andersson, M., Aastrup, T., Altun, S., Wallinder, D., Wallbing, L., Liangsupree, T., Riekkola, M.-L., Fornstedt, T., 2018. Anal. Chem. 90 (8), 5366–5374.

Galli Marxer, C., Collaud Coen, M., Greber, T., Greber, U.F., Schlapbach, L., 2003. Anal. Bioanal. Chem. 377, 578–586.

Gonda, A., Kabagwira, J., Senthil, G.N., Wall, N.R., 2019. Mol. Cancer Res. 17 (2), 337–347.

Gutgsell, A.R., Gunnarsson, A., Forssén, P., Gordon, E., Fornstedt, T., Geschwindner, S., 2022. Anal. Chem. 94 (2), 1187–1194.

Hao, S., Bai, O., Li, F., Yuan, J., Laferte, S., Xiang, J., 2007. Immunology 120 (1), 90–102.

Hemler, M.E., 2005. Nat. Rev. Mol. Cell Biol. 6, 801–811.

Kalluri, R., LeBleu, V.S., 2020. Science 367 (6478), eaau6977.

Karimi, N., Cvjetkovic, A., Jang, S.C., Crescitelli, R., Hosseinpour Feizi, M.A., Nieuwland, R., Lötvall, J., Lässer, C., 2018. Cell. Mol. Life Sci. 75, 2873–2886.

Liangsupree, T., Multia, E., Metso, J., Jauhiainen, M., Forssén, P., Fornstedt, T., Öörni, K., Podgornik, A., Riekkola, M.-L., 2019. Sci. Rep. 9 (1), 1–10.

Liangsupree, T., Multia, E., Riekkola, M.-L., 2021a. J. Chromatogr. A 1636, 461773.

Liangsupree, T., Multia, E., Saarinen, J., Ruiz-Jimenez, J., Kemell, M., Riekkola, M.-L., 2021b. Anal. Biochem. Submitted to.

Lim, H.J., Saha, T., Tey, B.T., Tan, W.S., Ooi, C.W., 2020. Biosens. Bioelectron. 168, 112513.

Liu, S., Zhang, H., Dai, J., Hu, S., Pino, I., Eichinger, D.J., Lyu, H., Zhu, H., 2015. MAbs 7 (1), 110–116.

Meldolesi, J., 2018. Curr. Biol. 28 (8), R435–R444.

Morelli, A.E., Larregina, A.T., Shufesky, W.J., Sullivan, M.L.G., Stolz, D.B., Papworth, G. D., Zahorchak, A.F., Logar, A.J., Wang, Z., Watkins, S.C., Falo, L.D., Thomson, A.W., 2004. Blood 104 (10), 3257–3266.

Müller, N., 2019. Front. Pharmacol. 10, 1251.

Multia, E., Liangsupree, T., Jussila, M., Ruiz-Jimenez, J., Kemell, M., Riekkola, M.-L., 2020. Anal. Chem. 92, 13058–13065.

Multia, E., Sirén, H., Andersson, K., Samuelsson, J., Forssén, P., Fornstedt, T., Öörni, K., Jauhiainen, M., Riekkola, M.-L., 2017. Anal. Biochem. 518, 25–34.

Multia, E., Tear, C.J.Y., Palviainen, M., Siljander, P., Riekkola, M.-L., 2019. Anal. Chim. Acta 1091, 160–168.

Premaratne, G., Mubarak, Z.H. Al, Senavirathna, L., Liu, L., Krishnan, S., 2017. Sensor. Actuator. B Chem. 253, 368–375.

Reina, M., Espel, E., 2017. Cancers 11 (9), 153.

Stubenrauch, K., Wessels, U., Essig, U., Kowalewsky, F., Vogel, R., Heinrich, J., 2013. J. Pharm. Biomed. Anal. 72, 208–215.

Suthar, J., Parsons, E.S., Hoogenboom, B.W., Williams, G.R., Guldin, S., 2020. Anal. Chem. 92, 4082–4093.

Termini, C.M., Gillette, J.M., 2017. Front. Cell Dev. Biol. 5, 34.

Tutanov, O., Proskura, K., Kamyshinsky, R., Shtam, T., Tsentalovich, Y., Tamkovich, S., 2020. Front. Oncol. 10, 2173.

Vitte, J., Pierres, A., Benoliel, A.-M., Bongrand, P., 2004. J. Leukoc. Biol. 76 (3), 594–602.

Vrhovac, L.S., Šelemetjev, S.A., Vatić, S., Mitrović, A., Milošević, J.R., Lolić, A., Beletić, A.D., Polović, N., 2021. Talanta 223, 121588.

Willms, E., Cabañas, C., Mäger, I., Wood, M.J.A., Vader, P., 2018. Front. Immunol. 9, 738.

Witwer, K.W., Théry, C., 2019. J. Extracell. Vesicles 8 (1), 1648167.

Xie, L., Jones, R.M., Glass, T.R., Navoa, R., Wang, Y., Grace, M.J., 2005. J. Immunol. Methods 304, 1–14.

Yong, T., Zhang, Xiaoqiong Bie, N., Zhang, H., Zhang, Xuting, Li, F., Hakeem, A., Hu, J., Gan, L., Santos, H.A., Yang, X., 2019. Nat. Commun. 10 (1), 1–16.

Zech, D., Rana, S., Büchler, M.W., Zöller, M., 2012. Signal 10 (1), 1–17.

Zhang, H., Freitas, D., Kim, H.S., Fabijanic, K., Li, Z., Chen, H., Mark, M.T., Molina, H., Martin, A.B., Bojmar, L., Fang, J., Rampersaud, S., Hoshino, A., Matei, I., Kenific, C. M., Nakajima, M., Mutvei, A.P., Sansone, P., Buehring, W., Wang, H., Jimenez, J.P., Cohen-Gould, L., Paknejad, N., Brendel, M., Manova-Todorova, K., Magalhães, A., Ferreira, J.A., Osório, H., Silva, A.M., Massey, A., Cubillos-Ruiz, J.R., Galletti, G., Giannakakou, P., Cuervo, A.M., Blenis, J., Schwartz, R., Brady, M.S., Peinado, H., Bromberg, J., Matsui, H., Reis, C.A., Lyden, D., 2018. Nat. Cell Biol. 20, 332–343.

Zhang, Y., Forssén, P., Fornstedt, T., Gulliksson, M., Dai, X., 2017. Inverse Probl Sci Eng 26 (10), 1464–1489.